Novel inorganic-organic perovskites for solution processable photovoltaics

Investigators
Michael D. McGehee, Professor, Materials Science and Engineering;
Hemamala Karunadasa, Assistant Professor, Chemistry; Eric T. Hoke, Research Staff, Geballe Laboratory for Advanced Materials; Colin D. Bailie, Andrea R. Bowring, Rebecca A. Belisle, Dan Slotcavage, PhD Researchers, Materials Science and Engineering; William H. Nguyen, Ian Smith, Abraham Saldivar, Adam Slavney, PhD Researcher, Chemistry; PhD Researchers, Chemistry; Emma R. Dohner, Undergraduate Researchers, Chemistry, Stanford University.

Abstract

We have fabricated semi-transparent perovskite solar cells with an efficiency of over 12%. This has enabled us to make 4-terminal hybrid tandem solar cells which comprise of a semi-transparent large bandgap $CH_3NH_3PbI_3$ perovskite solar cell stacked on top of a smaller bandgap CIGS or silicon solar cell, achieving efficiencies over 18% in the case of the CIGS-perovskite tandem. As the reliability of the perovskite material remains the greatest technical risk in commercialization of perovskite photovoltaics, we have made several important discoveries regarding instabilities of the perovskite to electrical bias and illumination. In particular, we have found that perovskite solar cells in planar architectures typically exhibit hysteresis with voltage, and a decline in performance under steady-state conditions that can be reversed by forward biasing the device. These observations are consistent with electromigration of ions within the device during operation. We have also found that larger bandgap perovskites incorporating mixed halides, such as $CH_3NH_3Pb(I_{1-x}Br_x)_3$, generally undergo a halide segregation process under illumination. This produces domains with a smaller bandgap than the starting material and limits the open circuit that can be achieved by these materials. We have previously shown that the $CH_3NH_3PbI_3$ perovskite is highly sensitive to moisture. We have developed 2-dimensional perovskite materials incorporating hydrophobic organic cations that have greatly improved the moisture resistance, with no degradation products observed after 46 days of moisture exposure.

Introduction

The objectives of this work are to design, synthesize and characterize new families of inorganic-organic perovskites for the application of low cost, hybrid tandem photovoltaics with efficiencies above 25%. For this application, the perovskite device needs to obtain high power conversion efficiencies over 15% and large open circuit voltages of over 1.2 V, be stable for many years and be safe for consumers and the environment. To meet these criteria, we are varying the stoichiometry of the inorganic constituents in the 3D perovskites as well as develop new layered (2D) perovskites to study the effect of the structure on the bandgap and electrical properties of the material and increase the open circuit voltage of devices. We are engineering perovskites with functionalized organic cations to promote stability of the material. We are also characterizing the optoelectronic properties of numerous lead-free perovskite materials to avoid the toxicity concerns of the lead-based perovskites.

Background

The efficiency of solution-processable perovskite solar cells has continued to advance at a rapid pace over the past year. After only a few years of research as photovoltaic material, devices based on the perovskite $CH_3NH_3PbI_3$ have in the past few months achieved certified power conversion efficiencies of over 20% in the laboratory[1] (**Figure 1**). Recent advances have involved further optimization of the perovskite ink solution and processing conditions to obtain a more uniform film morphology, and slight modifications to the perovskite stoichiometry to tune the perovskite bandgap and absorption onset.[2,3]

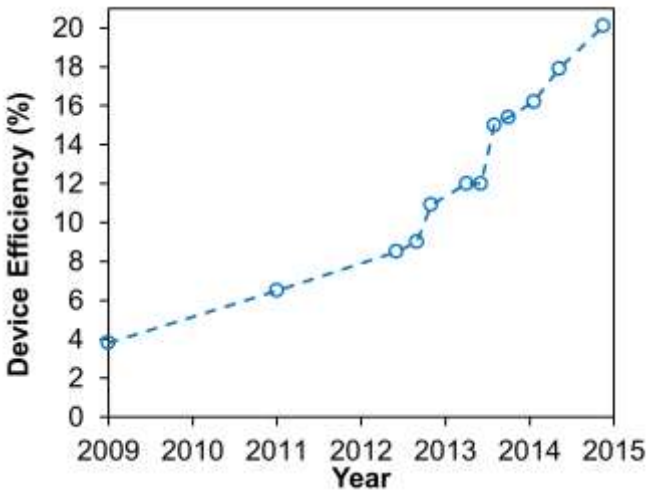

Figure 1: Efficiency of record lab-scale perovskite devices.

Hybrid perovskite materials have a relatively large optical bandgap (above 1.5eV for lead containing perovskites) and can obtain large open circuit voltages in excess of 1.1V.[2] This opens the possibility of making perovskite-silicon and perovskite CIGS tandem solar cell where the perovskite subcell absorbs the high energy photons and transmits lower energy photons to the CIGS or silicon device. A material with a bandgap of approximately 1.8 eV is needed to achieve current matching when paired with a conventional silicon solar cell. We and others[4] have previously demonstrated that the bandgap of $CH_3NH_3Pb(I_{1-x}Br_x)_3$, can be continuously tuned from 1.6 to 2.3 eV by replacing iodide with bromide.

Hybrid perovskite photovoltaics currently face significant stability challenges which pose the greatest technical risk towards the commercialization of these devices. The most commonly studied perovskites are hygoscopic and degrade in the presence of moisture. We show that this degradation mechanism can be significantly suppressed by adding hydrophobic layers to the perovskite,[5] and potentially can be solved with appropriately engineered module encapsulants. However, there is a growing body of evidence from our research and from other laboratories that ion migration occurs in the material in the presence of electric fields, and for mixed-halide composition perovskites, in the presence of light. Ion migration can cause changes in the electric field distribution in the device. This has been hypothesized to cause the output power of perovskite solar cells to

fluctuate and decline with time. Perovskite devices frequently exhibit hysteresis with voltage bias, which may also be a consequence of ion drift in the devices.

Results

In this report we first highlight our first demonstration of a mechanically stacked, 4-terminal tandem solar cell utilizing a semi-transparent perovskite device as the large bandgap junction. We also present our investigations into understanding the hysteresis and stability of perovskite devices under electrical bias, and the photo-stability of mixed-halide perovskites. We demonstrate improved stability to moisture using new layered perovskite materials. Most of the topics presented in this report have been published in peer reviewed journals over the past year that are listed in the Publications and Patents section of this report.

4-terminal, perovskite hybrid tandem photovoltaic solar cells

Perovskite solar cells have made rapid progress in the last few years at a pace unmatched by any other photovolatic technology. These thin film perovskite solar cells have primarily been developed for single-junction modules, but we feel the greatest advantage of this new material is the ability to make low-cost tandems using conventional low-bandgap materials in the bottom cell. All Si and CIGS modules have a glass cover sheet to provide transparency, mechanical rigidity, and environmental sealing. The opportunity now exists to expand the functionality of the cover glass by depositing a string of perovskite cells onto the glass (**Figure 2**). This upgrade to the cover glass and module is expected to improve the module efficiency by 15-30% (relative). On the timescale of 5 years, perovskite on high-quality Si tandems are expected to reach 30% efficiency. Since the layers of the perovskite cells can be printed at low cost with high-throughput tools, and the modules will not be substantially modified, we estimate the cost per area will only increase by ~5% and new factories will not be needed. By controlling the size of the perovskite cells, the separate top and bottom cell strings can be current-matched at the module level (**Figure 2**). This allows the module to be operated with only two wires leaving the module and requiring only a single system-level inverter.

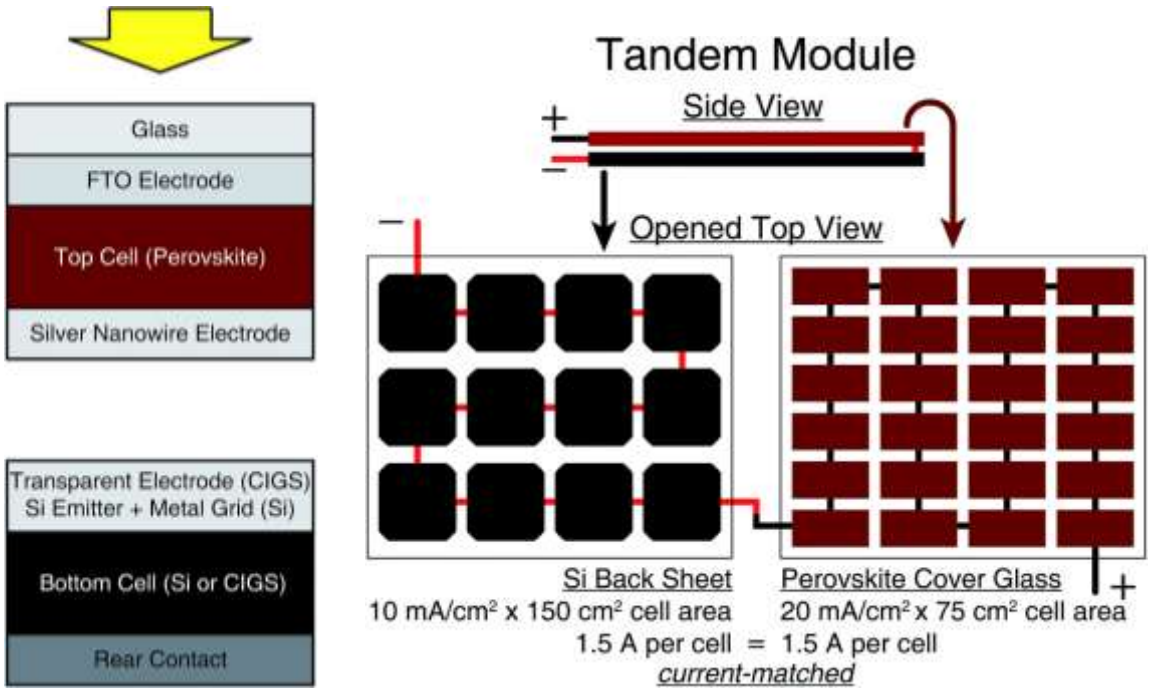

Figure 2: (Left) Schematic of a mechaniically-stacked tandem fabricated in this work with a perovskite solar cell as the top cell and Si or CIGS as the bottom cell. (Right) Current-matching at the module level. An example perovskite/silicon module with a simplified geometry and current density to demonstrate how current-matching at the module level can occur with a mechanically-stacked tandem. In this example module, the filtered silicon produces half the photocurrent density of the perovskite, so the silicon cells are twice as large to match the current of the perovskite cells. In this example, all cells are strung together in series; the total voltage of the module is the sum of the individual cell voltages.

Mechanically-stacked tandems require a semi-transparent top cell. The perovskite solar cell architecture used in this study uses a mesoporous titanium dioxide (TiO_2) layer infiltrated with the perovskite and contacted on either side by electron-selective (compact TiO_2) and hole-selective (2,2′,7,7′-tetrakis(*N*,*N*′-di-*p*-methoxyphenylamine)-9,9′-spirobifluorene, spiro-OMeTAD) contacts. For compatibility with these existing electron- and hole-selective contacts, we use the $MAPbI_3$ perovskite rather than the optically ideal $MAPbBrI_2$. $MAPbBrI_2$ was also not chosen due to a photo-instability observed in this material.[6] The transparent front electrode is fluorine-doped tin oxide (FTO) coated glass. Typically, a perovskite solar cell is opaque with an approximately 100 nm thick metal back electrode of either Au or Ag. This metal back electrode provides a low-resistance electrical contact and a reflective surface, giving the perovskite a second chance to absorb any light that was not absorbed on the first pass. To enable the transparency required to make a mechanically-stacked tandem, we needed a transparent top electrode.

The technical constraints that the top transparent electrode must meet are stringent. The electrode must be highly transparent in the critical 600–1000 nm window where the

perovskite is not absorbing all of the light and the bottom cell has significant external quantum efficiency (EQE). The sheet resistance of the transparent electrode should be at most 10 Ω/□ because the transparent electrode must have high lateral conductivity to minimize resistive loss when carrying the large current density generated in the perovskite cell. Perhaps most importantly, this electrode must be applied after deposition of the spiro-OMeTAD layer onto a temperature- and solvent-sensitive perovskite solar cell without damaging it. For these reasons, high-performance transparent conductive oxides widely used in industry cannot be directly sputtered onto a perovskite solar cell without a buffer layer. An electrode meeting these criteria has not been demonstrated before now. We use a silver nanowire (AgNW) mesh electrode which has been shown in other cases to have a low sheet resistance and high optical transmission and develop a new method of depositing this electrode onto our perovskite cell in a room-temperature solvent-free process. This AgNW electrode serves as the linchpin for our mechanically-stacked tandem architecture.

We first form our AgNW transparent electrode on a flexible polyethylene terephthalate (PET) film by spray deposition. The resulting AgNW film has a sheet resistance of 12.4 $\Omega/\square^{-1}$ and exhibits 90% transmission between 530 and 730 nm falling off to 87% at 1000 nm. The AgNW film is then completely and uniformly donated from the PET to the top spiro-OMeTAD layer of the perovskite solar cell by mechanical transfer ideally without damaging the sensitive AgNW or perovskite films. Because this is a research-stage procedure, the applied force of the mechanical transfer was manually rather than automatically controlled. Variability in the applied force can cause shorting (high pressure) as well as incomplete transfer (low pressure), resulting in a spread of device efficiencies. Automated precise control of the applied force is expected to remove these inconsistencies. As a result of the transfer, the conductivity of the AgNW film typically improves by 2 Ω/□. The primary reason for this increase in conductivity is the planarization of the AgNW film due to the downward force of the transfer lamination process, which reduces the resistance of junctions between wires.[7] A secondary effect is that the AgNWs have been embedded into the moderately conductive spiro-OMeTAD layer (10^{-3} S cm^{-1}) on top of the perovskite device. This transfer step decouples the fabrication of the perovskite solar cell from that of the electrode, allowing each to be optimized independently. Independent fabrication eliminates any thermal or solvent damage that the spiro-OMeTAD or perovskite may otherwise incur during the AgNW deposition process. We complete the semi-transparent solar cell by depositing two lithium fluoride (LiF) anti-reflective (AR) coatings, 133 nm onto the glass surface and 176 nm on top of the AgNW electrode to improve transmission through the device.

The current–voltage curves and metrics of the semi-transparent perovskite cells and opaque control devices are shown in **Figure 3**. The loss in absorption in the perovskite due to the removal of the opaque metal back electrode was offset by reduced reflection from the glass surface by the AR coating, yielding comparable J_{sc} between the semi-transparent and opaque cells. We note that if the opaque cell had an AR coating, it would have approximately 0.5 mA cm^{-2} higher photocurrent. We control our measurements for hysteresis in accordance with a paper by Unger *et al.*[8] We found a 5 s delay time between stepping the voltage and measuring current necessary to achieve steady state and remove any semblance of hysteresis. This procedure for removing hysteresis was corroborated and confirmed by NREL when a device was sent for certification. Shadow

masks were used to define the illuminated area of a device. Opaque devices were illuminated through a 0.12 cm^2 mask and semi-transparent devices were illuminated through a 0.39 cm^2 mask.

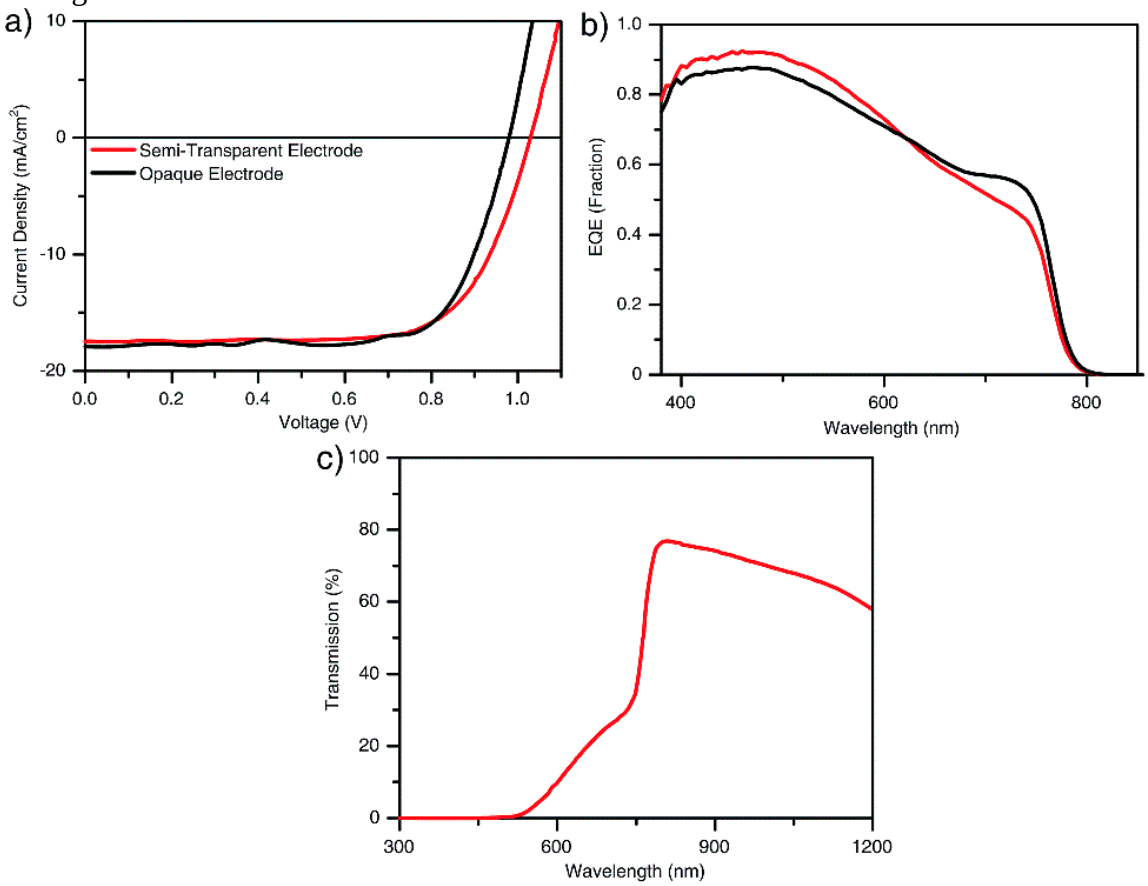

Figure 3: Perovskite device results. (a) Current–voltage curves comparing best opaque *vs.* semi-transparent perovskite devices. (b) EQE of semi-transparent device and opaque device. Note that the opaque device does not have AR coatings. (c) Transmission through semi-transparent perovskite with AR coatings. Peak transmission is 77% around 800 nm.

Figure 3c shows that the transmission through the semi-transparent device peaks at 77% around 800 nm, the center of the 600–1000 nm transmission window that is critical for tandems. Much of the transmission loss is due to parasitic absorption in the FTO electrode, AgNW electrode, and spiro-OMeTAD layer. Uniquely, our semi-transparent device has both a high below-bandgap transmission and a high efficiency. There remains significant room for improvement in the transmission. Low-temperature processes would allow for fabrication of the perovskite cell on ITO, which is more transparent than FTO. A more transparent hole-transporter than spiro-OMeTAD, which in its oxidized form absorbs light throughout the visible and infrared, would also improve transmission.

We have made tandems with both Si and CIGS as bottom cells. Both have a bandgap around 1.1 eV, which is sub-optimal for a single-junction solar cell but optimal for a double-junction tandem, and are commercially successful solar technologies. We use a 17.0% laboratory-scale CIGS device made using previously reported

procedures.[9] Although CIGS cells with 21% efficiency can be made, we chose a cell with a more modest efficiency for this demonstration to illustrate how cells that can be made at scale could be enhanced with a perovskite top cell. The current–voltage curves and external quantum efficiency of the semi-transparent perovskite solar cell, the CIGS solar cell and the CIGS solar cell underneath the perovskite solar cell are shown in **Figure 4**. To arrive at the efficiency of the 4-terminal tandem, the efficiency of the semi-transparent perovskite cell is added to the efficiency of the CIGS solar cell when underneath the perovskite cell. With our 12.7% semi-transparent perovskite cell, we improve the 17.0% CIGS cell to 18.6% in a tandem (**Table I)** as measured in-house. This cell was not sent for certification due to scratching of the electrode from excessive handling. A different cell was sent to NREL and was certified as 17.3% with an 11.7% semi-transparent perovskite cell which was slightly higher than our in-house measurement of 17.1%. The good agreement between the in-house and certified measurements lends credence to the other values reported herein.

Table I: Performance metrics of semi-transparent perovskite cell, CIGS cell, TI-Si cell, and the resulting tandem efficiencies

	J_{SC} (mA cm^{-2})	V_{OC} (mV)	FF (−)	Efficiency (%)
Semi-transparent perovskite	17.5	1025	0.71	12.7
TI-Si – unfiltered	29.3	582	0.667	**11.4**
TI-Si w/IR-ARC – filtered	11.1	547	0.704	4.3
Tandem w/perovskite + TI-Si				**17.0**
CIGS – unfiltered	31.2	711	0.768	**17.0**
CIGS – filtered	10.9	682	0.788	5.9
Tandem w/perovskite + CIGS				**18.6**

Perovskite solar cells are already efficient enough to upgrade the performance of silicon solar cells made with low-quality silicon using the polycrystalline tandem approach. Here, we explore lower-quality sources of Si including cast multicrystalline silicon (mc-Si) wafers made from feedstock with high impurity content recycled from the top 10% of other cast multicrystalline ingots (TI-Si) (**Figure 4** / **Table I**) and cast mc-Si wafers grown using 4.5 N (99.995% pure) upgraded metallurgical-grade Si (UMG-Si) instead of the more expensive Siemens-grade polysilicon (9 N, or 99.9999999% pure). Low-quality Si sources generally are not commercially viable today in single-junction devices because the material cost advantage of low-quality Si is offset by the reduction in performance due to impurities and crystal defects. We improve an 11.4% low-quality Si cell to 17.0% as a tandem, a remarkable relative efficiency increase of nearly 50%. Such a drastic improvement in efficiency has the potential to redefine the commercial viability of low-quality Si. Another tandem cell was sent to NREL for certification using a 17% silicon bottom cell. The tandem was certified as 17.9% efficient.

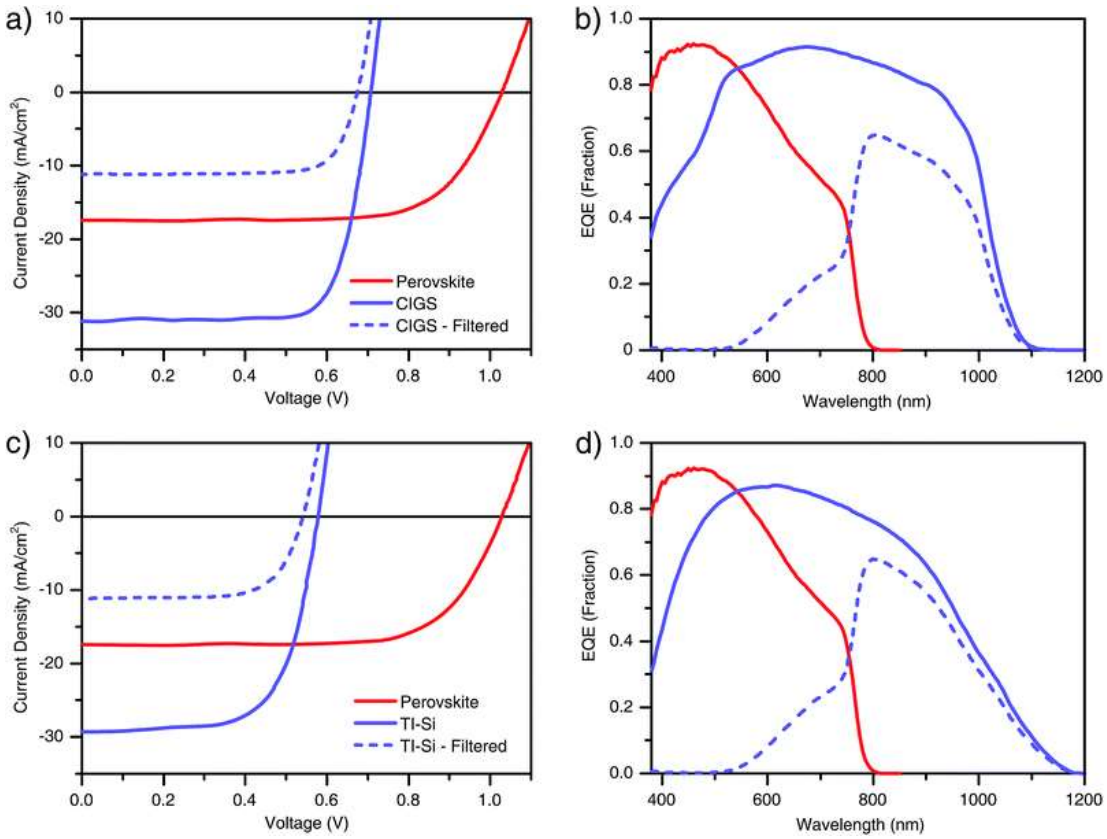

Figure 4: Perovskite and CIGS/Si tandem results. (a) Current–voltage and (b) EQE of semi-transparent perovskite cell, unfiltered CIGS cell, and CIGS cell filtered by the perovskite cell. (c) *IV* curves and (d) EQE of semi-transparent perovskite cell, unfiltered TI-Si cell, and TI-Si cell with an infrared-optimized anti-reflection coating filtered by the perovskite cell.

When making tandems as opposed to single-junction devices, some design parameters change for the bottom cell. The tandem relaxes the design constraints for both the Si and CIGS top layers. For example, the 20–50 nm CdS window layer used in commercial CIGS devices results in a photocurrent loss of 0.5 mA cm^{-2} due to reduced EQE from 400–550 nm caused by parasitic light absorption in the CdS layer. However, this does not affect the EQE of a tandem because the 400–550 nm light is already absorbed in the top cell, decoupling the optimization of the electronic and optical properties of the CdS layer. In single-junction Si cells, there is a strict tradeoff of the series resistance *vs.* EQE from 400–550 nm due to minority carrier recombination in the emitter layer. As the bottom cell in a tandem, the emitter thickness or doping can be increased without an EQE penalty. In this work, the Si has a 35 Ω/□ phosphorus-diffused emitter as opposed to 100 Ω/□ in industry. Lower sheet resistance in the emitter layer means bus bar spacing can be increased, reducing shading losses. The design parameters also change for the optimal anti-reflection coatings used in a tandem. All commercial solar cells use AR coatings to improve the transmission into the solar cell. For a single-junction cell, the AR coating on top of the cell is optimized for a broad spectral range from 400–1100 nm and necessarily

suffers in performance at the edges of this range. However, for the bottom cell in a tandem, the AR coating is optimized for a much narrower spectral range between 800 and 1100 nm, and can maintain a much higher performance through this narrower spectral range. Full consideration of the different design parameters between single-junctions and tandems such as these examples could yield further improvements in the future. Perovskite solar cells, in both their opaque and semi-transparent versions, are still in their infancy. As perovskite cells continue to improve, tandems employing them will directly benefit from these improvements. We note that the benefit of the tandem instead of a single junction cell is maximized when the top and bottom cells have approximately equivalent single-junction device performance. While we have not yet demonstrated a tandem that can compete directly in efficiency with record single-junction CIGS, Si, or perovskite cells, we estimate that converting the current record perovskite efficiency of 20.1% from an opaque to a semi-transparent cell and coupling it with a 21–22% single-crystal Si solar cell would result in a 25–27% efficient tandem. Before commercialization, issues pertaining to stability, yield, and the use of lead should be addressed. If the lead-based perovskite is found unsuitable for commercialization due to these issues, it may inspire the community to develop a new material that can be used as the high-bandgap semiconductor in a polycrystalline tandem.

Hysteresis and slow transient behavior in perovskite photovoltaics:

While reported efficiencies of perovskite solar cell have soared, there has been little debate in the literature about slow transient effects observed in perovskite-absorber devices that severely affect current–voltage measurements from which device performance metrics are commonly derived. Slow transients give rise to hysteresis between *IV*-measurements performed at different scan rates and directions, which can cause both over- and underestimated efficiency values. Hysteretic effects during *IV*-measurements have been observed in both mesoscopic[10] and thin-film perovskite photovoltaics.[11] In impedance measurements, illuminated perovskite-absorber devices exhibit an additional capacitance at low frequency caused by slow dynamic processes in the device that give rise to hysteresis in *IV*-measurements.[10,12] These effects can lead to erroneous device performance metrics if the slow device response is not considered during *IV*-measurements. Hysteresis in perovskite-absorber devices has been speculated to originate from trapping/de-trapping of charge carriers, changes in absorber or contact conductivity, ferroelectricity and ion migration.[10–12] Field-dependent orientation effects of the MA^+-dipoles and lattice distortion have been proposed to give rise to polarization effects that affect the charge carrier dynamics.[13] In addition, metal halides and metal halide perovskites can exhibit significant halide ion mobilities[14] that are often accelerated by photoexcitation.

We compared meso-porous titania based perovskite devices to solution-processed thin film devices. Hysteretic effects are observed in both type of architectures. We found that the device performance metrics derived from current–voltage measurements crucially depend on the scan direction and delay time after each voltage step before the measurement is taken. In **Figure 5**, *IV*-curves were measured with either a 10 ms or 5 s delay after each 50 mV voltage step.

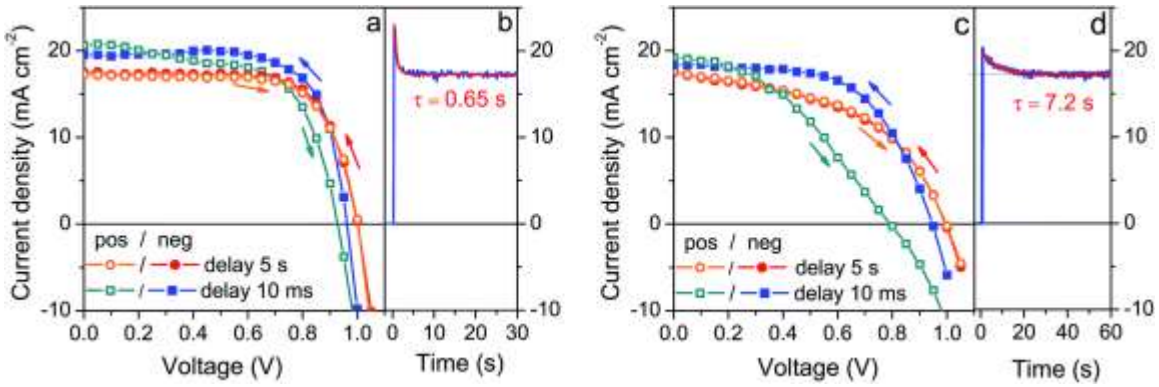

Figure 5: Current–voltage measurements of mesoporous-TiO_2 based perovskite-absorber device (a) and thin film device (c). Different scan directions (pos: 0 V to forward bias, neg: forward bias to 0 V) and delay times (0.01 s for fast scan and 5 s for slow scan) are compared. (b & d) Corresponding short-circuit current transients when switching the devices from V_{OC} to J_{SC} during illumination.

At a short delay time of 10 ms, significant hysteresis is observed for both the mp-TiO_2 based devices (**Figure 5a**) and the thin film devices (**Figure 5c**). For the mp-TiO_2 based device shown in **Figure 5**c, the efficiency at a 5 s delay time is 12.3% but would be overestimated to be 13.6% when measured with 10 ms delay time in the negative scan direction or underestimated to be 11.9% when measured rapidly in the positive scan direction. For the thin film device, measurement at 10 ms delay time in the negative direction results in an 11.2% device efficiency, while the scan in the opposite direction yields a power conversion efficiency of 6.07%. At a delay time of 5 s, the positive and negative scans converge with an efficiency of 8.5 ± 0.1%.

The meso-porous titania based devices exhibited less hysteresis and a weaker dependence of the device efficiency on the measurement delay time compared to the thin-film devices. On average, the meso-scopic devices exhibited a negative scan efficiency of 12.5% and 11.3%, using a delay time of 10 ms and 5 s, respectively. For the thin film devices investigated, the average device efficiency between a fast scan and slow scan in the negative scan direction was 10.1% *vs.* 6.7%.

We find that the conditions prior to the *IV*-measurement have a huge effect on the performance of thin film devices. After storage in the dark and prior to any light-soaking, thin-film devices often exhibited *IV*-curves with a slight s-shape and rather low performance as shown in (**Figure 6a**). Light-soaking at far-forward bias conditions ($J > 0$) dramatically improved the fill factor and photocurrent of this device leading to a power conversion efficiency increase from about 2% to about 4%. For some devices, we were able to further improve the device efficiency to about 7% by cycling the device between forward bias and 0 V under illumination several times prior to performing the *IV*-measurement. Illumination under reverse bias conditions, where the current flows in the opposite direction, had the opposite effect causing the *IV*-curves to become more s-shaped over time and the photocurrent to decrease. This can explain the observed slow decrease in short-circuit photocurrent with time. We found that we repeatedly improve or diminish the device efficiency by cycling the voltage bias conditions during light

soaking, indicating that there are reversible processes occurring in perovskite-absorber solar cells. In contrast, meso-porous titania based devices performed fairly independently of illumination and bias conditions prior to the measurements.

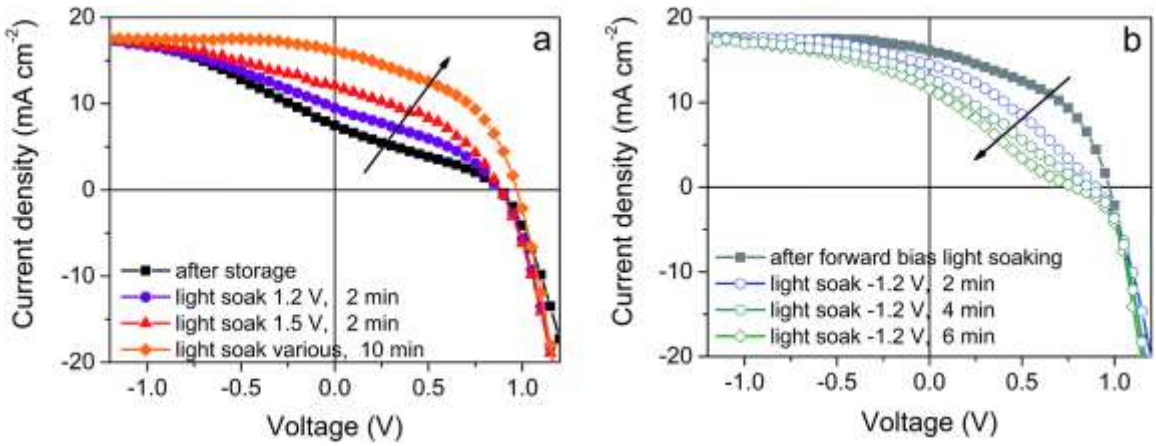

Figure 6: (a) Light-soaking at forward bias positively affects the current–voltage and hence the performance of thin film perovskite-absorber solar cells. (b) The reverse effect is observed after light soaking under reverse bias conditions with the *IV*-curves developing an s-shape.

The transient processes responsible for hysteresis appear to originate from the processes in the bulk of the perovskite-absorber. We have observed hysteresis in all of the perovskite device architectures that we have examined, irrespective of contact materials. When omitting the spiro-OMeTAD from our devices and contacting the perovskite-absorber directly with gold, hysteresis persisted. This suggests that hysteretic effects are neither solely caused by the perovskite/spiro-OMeTAD interface nor diffusion of Li^+, introduced to the device with the hole-transporting medium. We have found that contacts can influence the size and direction of the transients and hysteresis. Inverted thin film devices using PEDOT:PSS and $PC_{60}BM$ as hole and electron-selective contacts exhibit hysteresis at fast scan rates but the photocurrent appears to be lower rather than higher at fast scan rates. These observations are consistent with a mechanism where transient polarization of the perovskite absorber results in changes in charge carrier extraction efficiency at the carrier-selective contacts. In inverted devices, we found the photocurrent not to be as dependent on *IV*-scan delay time. This suggests that the charge extraction efficiency is not as severely affected by changes in perovskite polarization in these type of devices.

It is not yet clear whether the current transients in response to changes in the applied voltage have a similar origin to the slower processes occurring during pre-conditioning of the devices. The strong influence of bias pre-conditioning on *IV*-measurements suggests that polarization-induced changes in the device may play an important role in the observed current transients and device hysteresis. This polarization could be caused by diffusion of ionic species or alignment of methylammonium dipoles within the metal-halide lattice[10–13] under an applied voltage bias, resulting in changes in ability for photocurrent to be extracted from the device. Recent impedance studies on perovskite-absorber solar cells analyzing low-frequency phenomena observed slow transients with similar time-constants.[12] They arrive at a similar conclusion, that the observed

transiently higher photocurrent cannot be explained by charge-carrier accumulation but is likely due to ferroelectric MA^+ re-orientation and lattice distortion effects giving rise to polarized domains.

We propose that ion migration may also play a role in slower processes occurring during pre-conditioning of the devices. We suggest that photo-excitation of $MAPbI_3$ may enhance the ionic conductivity of the material, resulting in the observed transient currents and hysteresis when a bias is applied to the device. This process is well known to occur in metal halides, including PbI_2 where photo-excitation creates halide vacancies that enable the migration of halide ions.[15] Once these vacancies are created, an applied external bias can result in a redistribution of ions within the device, producing electric fields that aid or counteract charge carrier extraction. This can explain why under continuous illumination, the external quantum efficiency and photocurrent slowly decreases in perovskite solar cells and why applying a large forward bias to reverse the current direction causes the photocurrent to recover. Applying a reverse bias or short circuit conditions during illumination is expected to cause negatively charged ions such as I^- in the perovskite to migrate towards the titania cathode and positive ions such as MA^+ and Li^+ towards the hole-selective contact. This may create an extraction barrier for both electrons and holes at their respective contact, resulting in the observed s-shaped *IV* behavior (**Figure 6**). Forward-biasing the device during illumination can drive these ions in the opposite direction, potentially allowing the device photocurrent to recover if the pre-conditioning forward bias is applied for an adequate time. This redistribution of ions under illumination can explain why the current–voltage behavior of perovskite devices is sensitive to the pre-conditioning bias history before the measurement.

Since ion migration is particularly sensitive to the concentration of mobile vacancies (or interstitials depending on the mechanism), this proposed mechanism would suggest that the transient behavior of perovskite devices should be influenced by the precise stoichiometry of the perovskite material, as well as the degree of crystallinity and the size of crystalline domains. The significant differences in the transient behavior that we observed between the meso-scopic and thin-film devices may be a consequence of differences in stoichiometry or morphology due to the differences in processing. The thin film devices may contain trace amounts chloride due to the employed deposition procedure. As any ion migration will likely be detrimental for the long-term reliability of perovskite-absorber devices, reducing any ion-migratory effects in hysteresis may be an important step for improving long-term reliability.

Photostability of mixed-halide perovskites:

We investigated the opto-electronic properties of various compositions of the perovskite family $CH_3NH_3Pb(Br_xI_{1-x})_3$ to assess which stoichiometries are best suited for a tandem solar cell. One attractive attribute of hybrid perovskites as photovoltaic absorbers is the ability to continuously tune the absorption onset by alloying different halides into the structure. For example, the bandgap of $(MA)Pb(Br_xI_{1-x})_3$ ($MA = CH_3NH_3$) can be continuously tuned over the range 1.6–2.3 eV,[4] making these materials suitable both for single-junction solar cells and for the larger bandgap absorber of tandem solar cells. Photovoltaic devices containing $(MA)Pb(Br_xI_{1-x})_3$ have demonstrated PCEs of 4–16% for a wide range of halide ratios,[2,4,16–18] and an open circuit voltage (V_{OC}) of 1.5

V has been achieved using the largest bandgap perovskite of this family: (MA)$PbBr_3$.[19] Although solar cells containing (MA)PbI_3 have obtained V_{OC}'s of up to 1.15 V,[20] solar cells with mixed-halide perovskites have so far not produced the larger V_{OC}'s that may be expected from their larger bandgaps. Several groups have reported a decrease in V_{OC}, despite the increase in optical band gap, in (R)$Pb(Br_xI_{1-x})_3$ (R = CH_3NH_3 or $HC(NH_2)_2$) absorbers for $x > 0.25$.[4,16,17,21]

We examined the optical properties of (MA)$Pb(Br_xI_{1-x})_3$ thin films to understand the poor voltage performance of solar cells with the bromide-rich alloys. Surprisingly, for perovskites with $0.2 < x < 1$ we find that a second PL peak forms at ~1.68 eV and grows in intensity under continuous illumination (**Figure 7a**). The position of this new peak is independent of halide composition and bandgap (**Figure 7b**). After less than a minute of continuous visible-light soaking (argon ion laser, 457 nm, 15 mW/cm^2) the PL intensity from the new low-energy peak becomes more than an order of magnitude more intense than the original peak (**Figure 7c**). We find that this PL spectral change is not dependent upon the spectrum or coherence of the light source and that it occurs as long as the light is absorbed by the perovskite. Notably, these changes are reversible; the original PL spectra return after the materials are left in the dark for 5 minutes. Moreover, the spectra can be repeatedly cycled between these two states by turning on and off the excitation light (**Figure 7c**).

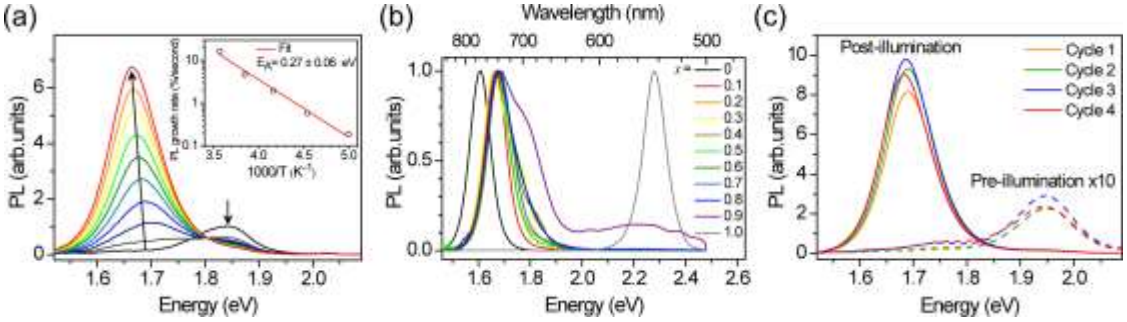

Figure 7: (a) Photoluminescence (PL) spectra of an $x = 0.4$ thin film over 45 s in 5-s increments under 457 nm, 15 mW/cm^2 light at 300 K. Inset: temperature dependence of initial PL growth rate. (b) Normalized PL spectra of (MA)$Pb(Br_xI_{1-x})_3$ thin films after illuminating for 5-10 minutes with 10-100 mW/cm^2, 457 nm light. (c) PL spectra of an $x = 0.6$ thin film after sequential cycles of illumination for 2 minutes (457 nm, 15 mW/cm^2) followed by 5 minutes in the dark.

To understand the origin of the new PL feature, we performed photocurrent spectroscopy measurements on photovoltaic devices containing (MA)$Pb(Br_xI_{1-x})_3$ before and after light soaking to characterize absorption from band-edge states (**Figure 8**). A new absorption shoulder forms around 1.7 eV after light soaking, which completely disappears after the devices are left in the dark for 1 h. We speculate that these new PL and absorption features in the light-soaked mixed-halide perovskites are due to the formation of small, iodide-enriched domains with a lower bandgap compared to the alloy. The absorption shoulder in the light-soaked $x = 0.6$ alloy has an absorption coefficient similar to the expected value if ~1% of the material converted into the $x = 0.2$ perovskite (**Figure 8**). The observations of this absorption shoulder and additional PL peak at 1.68

eV were recently reported for (MA)Pb($Br_{0.4}I_{0.6}$)$_3$ and were attributed to the existence of multiple phases.[22] However, the role of light soaking in producing these features was not examined.

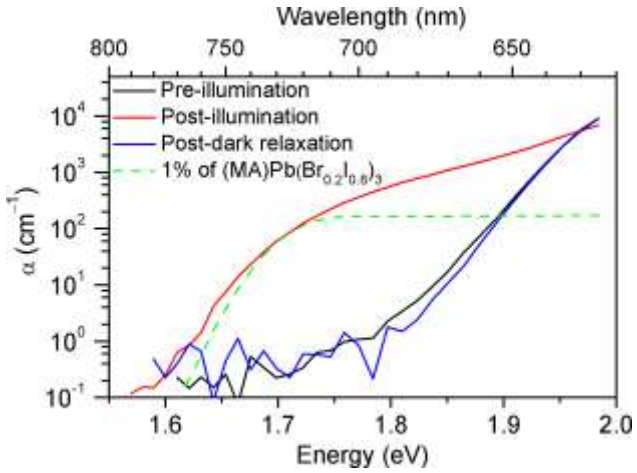

Figure 8: Absorption spectra of an x = 0.6 film before (black) and after (red) white-light soaking for 5 minutes at 100 mW/cm^2, and after 1 h in the dark (blue). A scaled absorption spectrum of an x = 0.2 film (dashed green) is shown for comparison.

In order to reversibly create iodide-rich domains, the bromide concentration should be slightly enhanced elsewhere in the films. To test this hypothesis, we performed XRD measurements on x = 0.6 thin films before and after light soaking. We observe splitting of all XRD diffraction peaks with light soaking, and regeneration of the original sharp diffraction patterns after the films are left in the dark (**Figure 9a**). Since perovskites with higher bromide content have a smaller lattice constant than those with higher iodide content, this splitting is consistent with the presence of a minority phase with significantly enhanced (x~0.2) iodide content and a majority phase with slightly enhanced bromide content (x~0.7) compared to the original material (**Figure 9b**). These phase compositions would suggest that the minority phase is about 20% of the material in these particular samples. If we compare the magnitude of XRD intensity from the two phases, we estimate that the minority phase makes up 23% of the material, after accounting for differences in structure factor for the two hypothesized phases. These values are substantially higher than the 1% minority phase estimated from the absorption measurements by photocurrent spectroscopy on mesoporous devices (**Figure 8**). We suggest that differences in morphology between the mesoporous devices and planar thin films may be responsible for the different minority phase yields under similar illumination conditions.

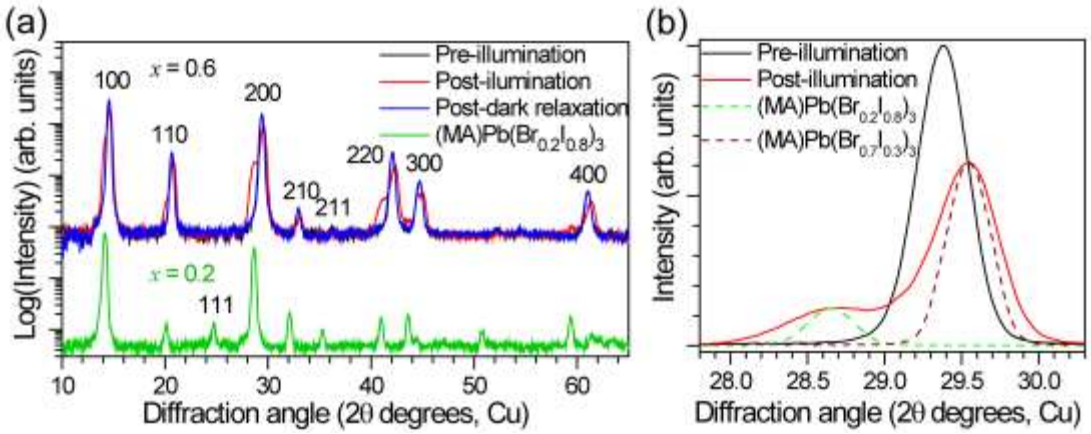

Figure 9: (a) XRD pattern of an x = 0.6 film before (black) and after (red) white-light soaking for 5 minutes at ~50 mW/cm^2, and after 2 h in the dark (blue). The XRD pattern of an x = 0.2 film (green) is offset for comparison. (b) The 200 XRD peak of an x = 0.6 film before (black) and after (red) white-light soaking for 5 minutes at ~50 mW/cm^2. XRD patterns of an x = 0.2 film (dashed green) and an x = 0.7 film (dashed brown) are included for comparison.

We monitored the PL spectral evolution under constant illumination at different temperatures to study the kinetics of this conversion. The low-energy PL peaks also form below room temperature (200 – 280 K), indicating that the spectral change is due to photoexcitation and not heating from the light. The initial growth rate in the low-energy PL peak follows Arrhenius behavior with an activation energy of 0.27 ± 0.06 eV (**Figure 7a**, inset). This value is similar to the activation energies attributed to halide migration in the perovskites $CsPbCl_3$, $CsPbBr_3$, $KMnCl_3$, $CuCdCl_3$, $KPbI_3$, $CuSnI_3$, and $CuPbI_3$, which span the range 0.25–0.39 eV.[14,23–25] Light-induced halide migration has also been reported to occur in metal halides such as $PbBr_2$ and PbI_2,[15,26] and is the basis for latent image formation in photography using AgI.[27] While halide mobilities in hybrid lead-halide perovskites have not yet been reported, ion conductivities of 7×10^{-8} and 3×10^{-9} S/cm have been reported for $KPbI_3$ and $CuPbI_3$, respectively.[23] Since the $(MA)Pb(Br_xI_{1-x})_3$ valence band is dominated by contribution from the halide p orbitals,[28] we speculate that formation of iodide-enriched domains stabilizes holes, which could provide a driving enthalpy for halide segregation under illumination (**Figure 10**). When these trapped holes are filled, entropy and lattice strain may cause the phase segregated material to relax back to the well-mixed alloy. Light-induced, reversible structural changes in $PbBr_2$ have been attributed to self-trapping of such photogenerated holes.[29] Alternatively, since iodide-rich domains have a smaller bandgap, they lower the energy of excitons, which could drive halide segregation. It is not yet clear whether these structural and spectroscopic changes can be induced by electrical excitation. Spectrally stable red-emitting $(MA)PbBr_2I$ LEDs have been recently demonstrated.[30] This suggests that the application of an electrical bias might not produce the large changes in emission that are observed under photoexcitation and that photogenerated excited states may play an important role in the transformation mechanism. It is also not

yet clear why photo-induced defects resemble the $x = 0.2$ perovskite for a range of bulk perovskite stoichiometries.

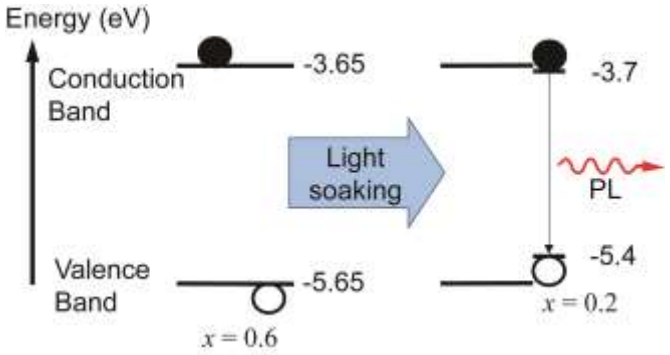

Figure 10: Schematic of the proposed mechanism for photo-induced trap formation through halide segregation. Photogenerated holes or excitons may stabilize the formation of iodide-enriched domains which then dominate the photoluminescence. The valence band (VB) and conduction band (CB) energies with respect to vacuum were estimated by interpolation of published values obtained from ultraviolet photoemission spectroscopy (UPS) and inverse photoemission spectroscopy (IPES) for the endpoint stoichiometries.[31]

This ion-transport mechanism suggests that crystallite size and quality should influence its kinetics. Accordingly, we have seen variations between samples in the rate of their light-induced changes. We see the growth of the low-energy PL even in single crystals of (MA)Pb(Br_xI_{1-x})$_3$, indicating that significant grain boundaries or surface defects are not required for this transformation. We have also observed this new phase upon light exposure (for both white LED and 457 nm excitation at 10–100 mW/cm^2) in (MA)Pb(Br_xI_{1-x})$_3$ thin films formed from a $PbCl_2$ precursor,[16] sequentially-deposited dip-converted[17] and vapor-converted[32] thin films, and in ($HC(NH_2)_2$)Pb(Br_xI_{1-x})$_3$ thin films,[21] all processed following the procedures described in the references. Approx. 10 s of continuous visible-light soaking at 10 mW/cm^2 (0.1 J/cm^2) was typically required for these PL spectral changes. We postulate that previously reported PL studies on mixed-halide perovskites,[21,22,33] in many cases done with ultrafast pulsed excitation, may have used much smaller light-soaking dosages that were insufficient to produce these changes.

In summary, we have observed the formation of a new low energy PL feature upon light soaking of (MA)Pb(Br_xI_{1-x})$_3$ and other mixed-halide perovskites. This spectral change, accompanied by the growth of sub-bandgap absorption states and a splitting of XRD peaks, is consistent with photo-induced halide segregation. In the case of (MA)Pb(Br_xI_{1-x})$_3$ solar cells, the red-shift in PL upon light illumination indicates a reduction in the electronic bandgap and quasi-Fermi level splitting, reducing their achievable V_{OC}'s. This photo-induced instability suggests that significant halide migration can occur in the perovskite, which we expect has serious implications for the stability of perovskite photovoltaics. We are planning to continue to study the mechanism of light-induced trap formation to better understand its potential impact on device

reliability, and access strategies to mitigate it. The results from this study indicate that the perovskite compositions (MA)Pb(Br_xI_{1-x})$_3$ with $0 \leq x \leq 0.2$, or x=1 that do not undergo halide segregation are best suited for making perovskite tandems.

A Layered Hybrid Perovskite Solar Cell Absorber with Enhanced Stability Towards Atmospheric Moisture

Along with developing absorbers containing less toxic materials, we are also working on optimizing the lead-based perovskite absorbers. As solar cells with perovskite absorbers reach commercially viable efficiencies, their stability to manufacturing and operating conditions must also be considered. The lead-iodide perovskites decompose upon exposure to relative-humidity levels as low as 11% over several days. We are functionalizing the organic groups in these materials to improve their moisture resistance.

Motivated by our observations that the structurally related two-dimensional perovskites readily formed high-quality films that appeared more resistant to humidity than the three-dimensional analogs, we sought to assess if the layered materials could act as solar-cell absorbers. Here, we show that the layered perovskite $(PEA)_2(CH_3NH_3)_2[Pb_3I_{10}]$ (**1**, PEA = $C_6H_5(CH_2)_2NH_3^+$) can serve as an absorber in a solar cell with an open-circuit voltage of 1.15 V and a PCE of 3.6%. Although our first-generation devices have lower efficiencies than those with three-dimensional perovskite absorbers, the layered structure brings distinct advantages. High-quality films of **1** can be easily deposited through one-step spincoating under ambient conditions and annealing steps are not required for device processing. These films are far more resistant to moisture compared to $(CH_3NH_3)[PbI_3]$, and do not require anhydrous conditions for device processing or operation.

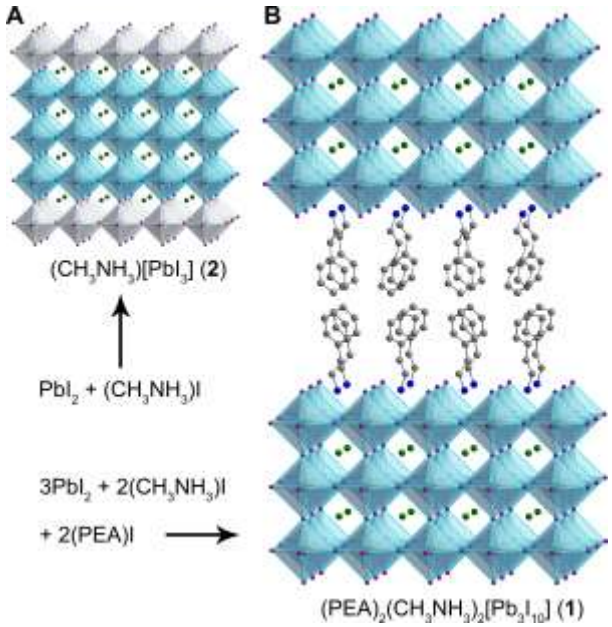

Figure 11: A) Structure of the three-dimensional perovskite $(CH_3NH_3)[PbI_3]$ and B) a model of the two-dimensional perovskite $(PEA)_2(CH_3NH_3)_2[Pb_3I_{10}]$ that can be derived from the three-dimensional structure by slicing along specific crystallographic planes (turquoise sheets in A). Turquoise, purple, blue, and gray spheres represent Pb, I, N, and C atoms, respectively. Disordered $CH_3NH_3^+$ groups are shown as green spheres. (PEA = 2-phenylethylammonium).

The layered perovskite structure can be derived from the three-dimensional analog by slicing along specific crystallographic planes.[34,35] The thickness of the inorganic layers can be controlled by choice of organic cation. Each inorganic layer in **1** consists of three sheets of corner sharing Pb-X octahedra (denoted $n = 3$). The structure contains two types of organic cations: the smaller $CH_3NH_3^+$ molecules fit in the cavities defined by eight corner sharing Pb-I octahedra while the larger phenethylammonium (PEA = $C_6H_5(CH_2)_2NH_3^+$) cations form an ordered bilayer that templates the inorganic layers (Figure 11). Reducing the dimensionality of the inorganic components from the three-dimensional structure causes an expected increase in bandgap. The n = 1, 2, and 3 structures have bandgaps of 2.4, 2.2, and 1.8 eV, respectively. We chose the n = 3 material for this study as it has the closest bandgap to the three-dimensional perovskite while affording new properties emerging from the hybrid layered structure. While this bandgap is larger than the ideal value of 1.4 eV calculated to be the Shockley-Queisser limit[36] it can absorb a significant fraction of the solar spectrum. It is also the ideal value for the higher bandgap absorber in a tandem solar cell, which can exceed the Shockley- Queisser limit.

Layered perovskites form oriented films on substrates through simple one-step dropcasting or spincoating techniques. Unlike $(CH_3NH_3)[PbI_3]$ that crystallizes as dodecahedra at room temperature, **1** forms plates indicating faster crystal growth in the *ab* plane along the inorganic sheets. Powder x-ray diffraction (PXRD) patterns of **1** on glass or titania substrates show only *00l* reflections revealing long-range order along the crystallographic *c* axis perpendicular to the inorganic sheets. Similar processing of three-dimensional perovskites do not afford continuous films. Films of comparable quality of $(CH_3NH_3)[PbX_3]$ can be obtained by thermal evaporation, or two-step vapor- or dip-conversion from PbI_2 or $PbCl_2$. In contrast to the three-dimensional analogs, the layered perovskites do not require high-temperature annealing for good device performance, allowing for simpler device fabrication.

The crystal structure of **1** has not been reported. Our crystallization attempts only afforded polycrystalline powders. By examining the crystal structures of $(CH_3NH_3)[PbI_3]$ and $(PEA)_2(CH_3NH_3)[Pb_2I_7]$ (the $n = \infty$ and n = 2 analogs of **1**, respectively) we can estimate the *d* spacing (distance between equivalent inorganic sheets) of **1** as ca. 29 Å. Low-angle reflections corresponding to such a long *c* axis were not evident in the PXRD patterns of oriented films. Therefore, we obtained unoriented PXRD patterns from pulverized powders of **1**. Here, low-angle reflections at 9.8°, 12.11°, and 15.60° match the third-, fourth-, and fifth-order reflections from the principle (*h*00) planes expected for a 29-Å cell axis. Furthermore, the unoriented PXRD pattern of **1** is similar to that of $(BA)_2(CH_3NH_3)_2[Sn_3I_{10}]$ (BA = butylammonium): the only n = 3 perovskite characterized

by single-crystal x-ray diffraction.[34] The electronic absorption spectrum of **1** shows an exciton band at 720 nm. When excited at 500 nm, the emission spectrum shows a sharp peak at 756 nm. As expected, this emission energy lies between the emission maxima for layered perovskites with lower values of n (n = 1 at 527 nm and n = 2 at 725 nm) and the three-dimensional perovskite ($n = \infty$ at 781 nm).

Devices utilizing **1** as the absorber were constructed using a typical perovskite-based device architecture employing TiO_2 and 2,2′,7,7′-tetrakis-(*N*,*N*-di-*p*-methoxyphenylamine)9,9′-spirobifluorene (spiro-OMeTAD) as the electron- and hole-selective contacts, respectively. Films of **1** were deposited from a *N*,*N*-dimethylformamide solution containing stoichiometric quantities of PbI_2, $(CH_3NH_3)I$ and (PEA)I using a single spin-coating step. Importantly, films of **1** can be processed under ambient humidity levels, which do not degrade the films. This allows for easier device processing compared to $(CH_3NH_3)[PbI_3]$ films, which require anhydrous deposition conditions, and multistep deposition methods,[37] or high-temperature annealing steps. A scanning-electron microscopy (SEM) image of the full device is shown in Figure 12. Typical thicknesses of the layers of TiO_2, **1**, Spiro-OMeTAD, and gold are 50, 450, 125, and 60 nm, respectively.

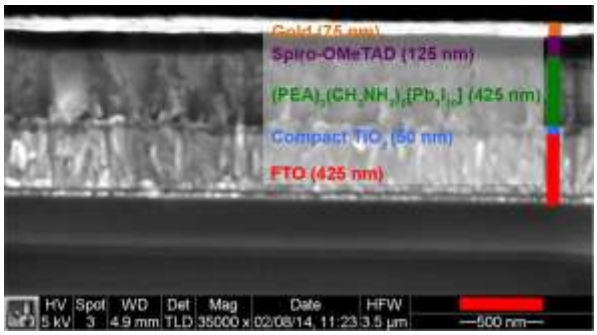

Figure 12: SEM cross section of planar devices utilizing 1 as the absorber layer.

We obtained *JV* curves of these devices using simulated AM1.5 solar illumination (Figure 13). The open-circuit voltages (V_{oc}) for these devices routinely exceed 1.0 V; the best devices show a value of 1.15 V. Owing to the larger bandgap of the two-dimensional material, these V_{oc} values are higher than for optimized cells containing $(CH_3NH_3)[PbI_3]$[37] These devices display fill factors of ca. 0.65 and afford a maximum power of 3.6 mW/cm^2 for 100 mW/cm^2 solar intensity, resulting in a 3.6% PCE. The current density under short-circuit conditions (J_{sc}) is ca. 5 mA/cm^2. Slow scan rates were used for these measurements to avoid current from capacitive cell charging and similar *JV* profiles were obtained for both forward and reverse scans (**Figure 13**). An external-quantum efficiency (EQE) of 50% was obtained for devices illuminated by monochromatic light and the integrated photocurrent density from these measurements matched the J_{sc} obtained from voltammetry corroborating the efficiencies calculated using the *JV* curves. Faster scan rates for the *JV* curves afforded currents as high as 11.5 mA/cm^2, but these voltammograms showed large hysteresis between forward and reverse scans and the higher PCEs of 6.1% calculated through these measurements were not

matched by the EQE measurements. The layered structure of the material likely affects charge extraction from these devices as carrier transport in the inorganic sheets is highly anisotropic, with no direct path between inorganic layers. Low-dimensional inorganic materials have previously been effectively used in photovoltaic devices,[38,39] and device optimization should afford improvements in J_{sc} and overall efficiency.

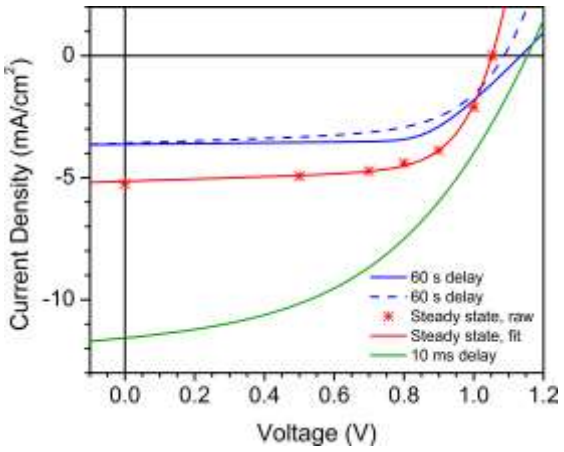

Figure 13: Current-potential (*JV*) curves of planar devices utilizing 1 as the absorber. The highest PCE, V_{oc}, and J_{sc} values were measured using fast voltage changes (green). Slower scans (blue) match more closely with steady-state values (red), achieving PCEs of 3.6%.

Upon exposure to humid atmospheres at room temperature, black $(CH_3NH_3)[PbI_3]$ converts to a bright-yellow solid that has been formulated as the hydrated structure $(CH_3NH_3)_4[PbI_6]\cdot 2H_2O$.[40] The tetragonal phase of $(CH_3NH_3)[PbI_3]$, which is the stable structure at room temperature, is prone to this reactivity with water, whereas the high-temperature cubic phase is more resilient.[4] To assess the stability of **1** and $(CH_3NH_3)[PbI_3]$ to humidity we used spincoated films of both materials on glass substrates. These films were exposed to relative-humidity levels of 11% and 54% and their PXRD patterns were periodically recorded (**Figure 14**). When exposed to 54% relative humidity the PXRD patterns of the three-dimensional perovskites show a new phase after just one day, and no reflections corresponding to the perovskites are visible after a five-day exposure. The new reflections cannot be indexed to the PXRD patterns of PbI_2, $(CH_3NH_3)I$, or $(CH_3NH_3)_4PbI_6\cdot 2H_2O$. The films became yellow and transparent upon full conversion to this new phase. This indicates a higher bandgap material, which would decrease device performance. In contrast, the PXRD pattern of **1** does not show additional reflections until six days and the perovskite phase remained dominant up to 20 days when the experiment was terminated. In 11% relative humidity the PXRD patterns of the three-dimensional perovskites show the emergence of the new phase in one day, while the PXRD pattern of **1** does not show additional reflections up to 15 days.

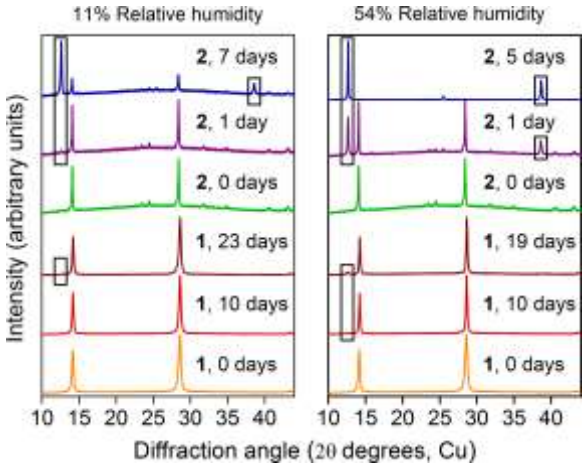

Figure 14: Powder x-ray diffraction patterns of films of $(CH_3NH_3)[PbI_3]$ and 1 after exposure to 11% (left) and 54% (right) relative-humidity levels. Reflections corresponding to decomposition products are boxed. Films of 1 maintain their crystal structure for more than 20 days while the 3D perovskite films begin degrading after 1 day and decompose after 5-7 days.

Our work shows that the two-dimensional organic-inorganic perovskite $(PEA)_2(CH_3NH_3)_2[Pb_3I_{10}]$ (**1**) can act as a solar cell absorber. The larger bandgap affords a higher open-circuit voltage of 1.15 V compared to devices with $(CH_3NH_3)[PbI_3]$ as the absorber. Solar cells containing **1** display fill factors of 0.65 and device efficiencies of up to 3.6%. Though devices containing the three-dimensional perovskites have exceeded efficiencies of 15%, their stability to reaction with water remains a concern. The two-dimensional structure, templated by organic cations, allows for high-quality films to be deposited on planar substrates using simple one-step spin-coating. Importantly, these films show much greater resistance to moisture compared to $(CH_3NH_3)[PbI_3]$ and do not require anhydrous processing or operating conditions. Further improvements to both material structure and device engineering should increase the PCE values of devices with layered perovskites. This platform may also allow for structural tuning at the molecular level. For example, hydrophobic groups in the organic layers could increase stability to moisture, conjugated organic layers could facilitate charge transport between inorganic sheets, and organic photosensitizers could improve the absorption properties of the material.

Post-synthetic Halide Exchange in (MA)[PbX$_3$] Perovskites

The three dimensional (3D) lead halide perovskite family of materials, $(A)[PbX_3]$ (A = small organic cation, X = Cl, Br, I) demonstrate many favorable qualities for optoelectronic applications. Their optical bandgaps can be varied from the near infrared (IR) to the ultraviolet (UV), accessing energies in-between by selecting which organic cations and halide anions to incorporate into the structure. Additionally, they can be designed to have free carriers, which would be ideal for a solar cell, or tightly bound excitons, which works well for emissive devices. To develop optoelectronic devices that

incorporate these materials, such as photovoltaics, light-emitting diodes (LEDs), and lasers, high-quality thin films are necessary in order to maximize the optical and electronic utility. For example, solar cell absorbers should cover the substrate to maximize optical absorption as well as to avoid electronic shunts between the adjacent layers. Such high-quality films of (MA)[PbI_3] (MA = $CH_3NH_3^+$) have been formed through many different synthetic routes, including vapor deposition, single-step solution processing, and multi-step solution processing. For (MA)[PbX_3] (X = Cl, Br), however, such high-quality films are not as easily obtained. In order to access higher voltages for solar cells, and for the construction of the higher bandgap absorber in a tandem solar cell, there is considerable interest in (MA)[$PbBr_3$] absorbers.

We have developed a new synthetic technique that uses the redox reactivity of the halides in Pb-X perovskites to exchange halides to achieve high-quality films of Pb-Br and Pb-Cl perovskites. The reduction potentials of I_2, Br_2, and Cl_2 (0.54, 1.07, and 1.36 V vs. SHE, respectively) dictate the reactivity in these reactions; chlorine can oxidize I^- and Br^- ions to I_2 and Br_2, respectively, and Bromine can oxidize I^-. By exposing high-quality films of Pb-I perovskite to dilute Cl_2 or Br_2 gas, we obtain a Pb-Cl or Pb-Br perovskite film of similar quality (**Figure 15**). This provides an easy method for producing device-quality films of 3D perovskites that were not easily obtainable before, without the need for further annealing or purification steps. A manuscript describing this work has been submitted for publication ("Post-synthetic halide conversion and selective halogen capture in hybrid perovskites" Solis-Ibarra, D.; Smith, I. C.; Karunadasa, H. I. manuscript under review).

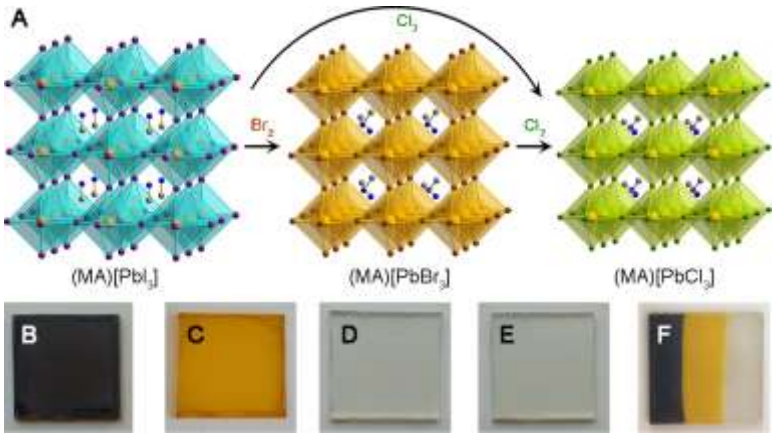

Figure 15: A) Reaction of 3D perovskites (MA)[PbX_3] (MA = $CH_3NH_3^+$, X = I and Br) with Br_2 and Cl_2 gas. Pb: orange, I: purple, Br: brown, Cl: green, N: blue, C: gray. Photographs of B) a (MA)[PbI_3] film, C) a (MA)[$PbBr_3$] film prepared by exposing a (MA)[PbI_3] film to Br_2 gas, D) a (MA)[$PbCl_3$] film prepared by sequentially exposing a (MA)[PbI_3] film to Br_2 and Cl_2 gas, and E) a (MA)[$PbCl_3$] film prepared by exposing a (MA)[PbI_3] film to Cl_2 gas. F) A film of all three perovskites formed by exposing parts of a (MA)[PbI_3] film to Br_2 and then to Cl_2 using a mask.

High-coverage films of (MA)[PbI_3] can be easily formed under ambient conditions by first spin-coating a PbI_2 film on a clean fluorine doped tin oxide (FTO) substrate and then

converting it to the perovskite by adding dropwise a solution of (MA)I. The transparent yellow PbI_2 films first turn a pale red color and then finally opaque black as the perovskite is formed. The films were annealed at 100 ºC for 15 minutes to complete the process. The perovskite structure (MA)[PbI_3] was confirmed by powder X-ray diffraction (PXRD), while film quality was confirmed by imaging the film using a scanning electron microscope (SEM, **Figure 16a**). Importantly, the films show complete coverage of the perovskite grains on the surface of the substrate and are similar to films described in literature that produce high-efficiency devices. Conversion of these films using Br_2 or Cl_2 gas allows for the formation of (MA)[PbX_3] (X = Br or Cl) films without loss of film quality (Figure **Figure 16d,e**).

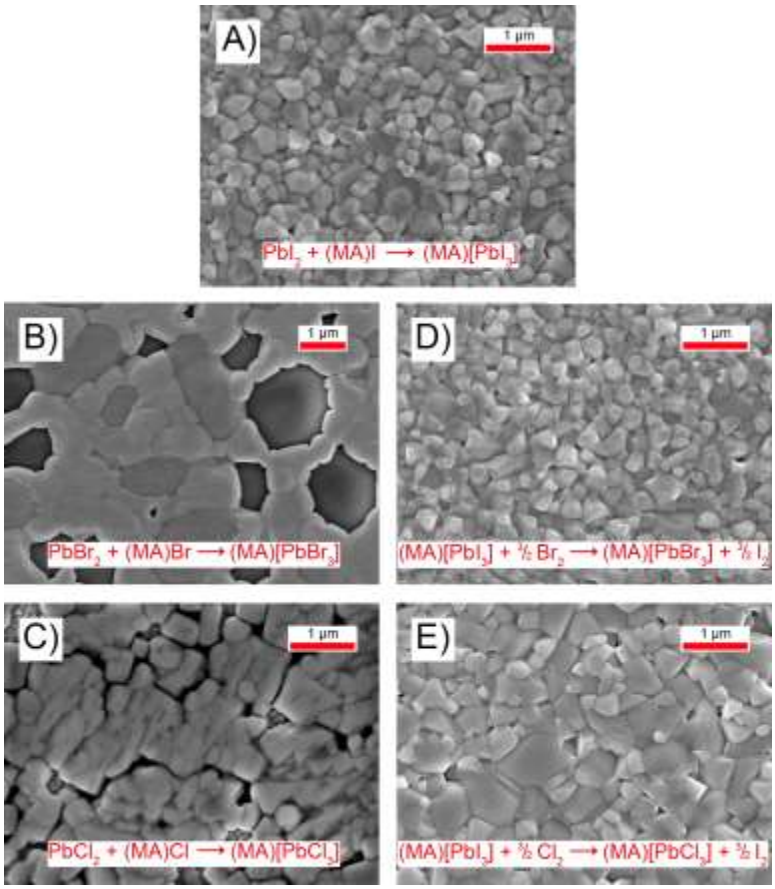

Figure 16: SEM images of 3D perovskite films. Films prepared from PbX_2 and (MA)X solutions (X = I, Br, or Cl): A) (MA)[PbI_3], B) (MA)[$PbBr_3$], and C) (MA)[$PbCl_3$]. Films formed by reaction of (MA)[PbI_3] films with X_2 gas (X = Br or Cl): D) (MA)[$PbBr_3$] and E) (MA)[$PbCl_3$].

To convert the perovskite film using halogen vapor, gas flow meters were used to combine a dry nitrogen stream with a concentrated stream of Cl_2 or Br_2 vapor to dilute it by a known amount (ca. 400× for Br_2 and ca. 500× for Cl_2). This dilute halogen vapor was passed over a film of (MA)[PbI_3] for 5-10 min, or until complete color change to orange/yellow (Br) or colorless (Cl) was observed. The product perovskite was confirmed

with PXRD (**Figure 17a**) and UV-Vis absorbance. Notably, the intensity of the diffraction peaks increases after this method despite not performing any annealing (**Figure 17b**). The quality of the resulting converted films were studied with SEM (**Figure 16d,e**). They are significantly better than independently prepared (MA)[$PbCl_3$] or (MA)[$PbBr_3$] films synthesized from lead chloride or lead bromide precursors, respectively (**Figure 16b,c**).

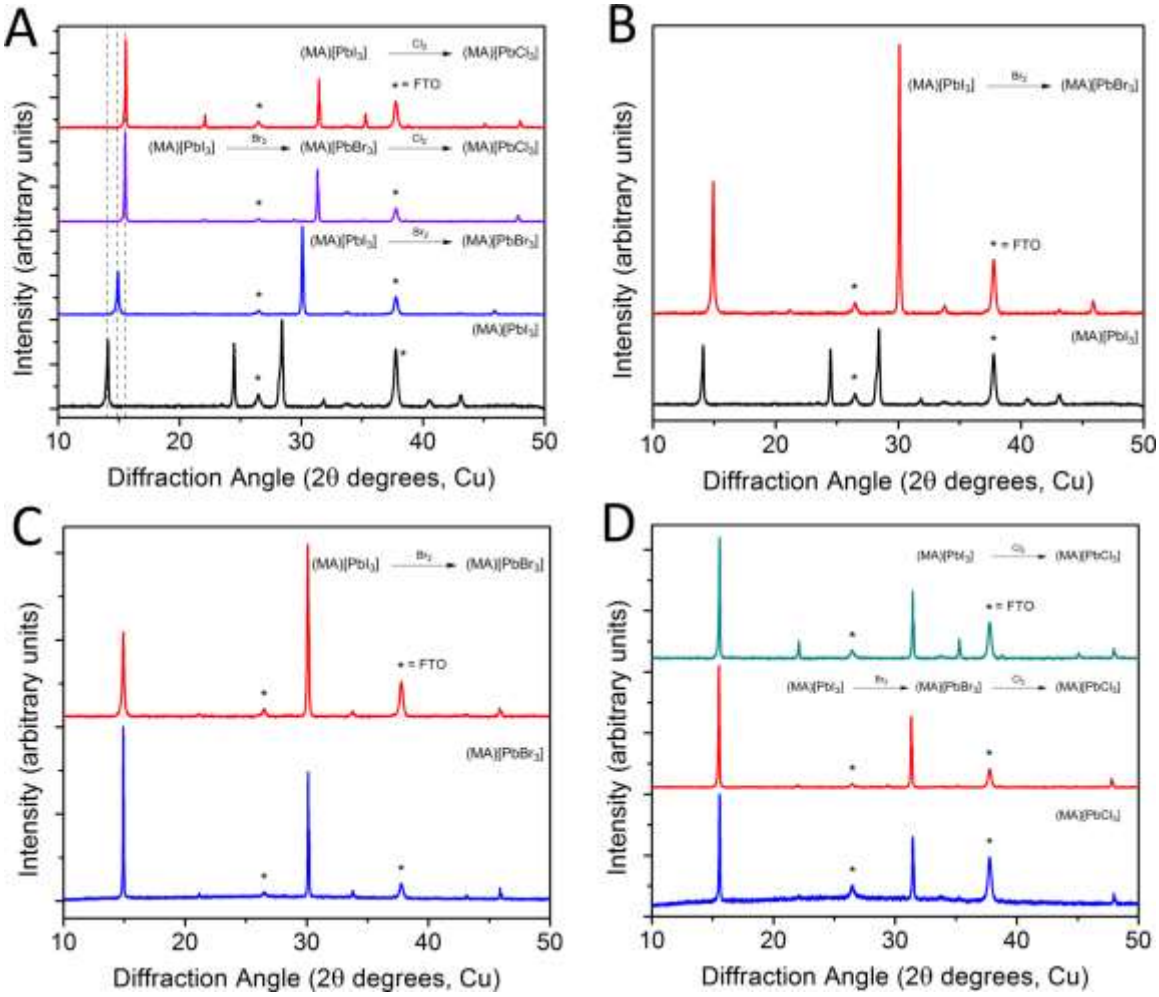

Figure 17: PXRD scans of the spin converted (MA)[PbX_3] films. A) The starting (MA)[PbI_3] film (black) and it's reaction products with Br_2 (blue), sequential Br_2 and Cl_2 (purple), and Cl_2 (red). B) Example of crystallinity improvement upon conversion of (MA)[PbI_3] (black) with Br_2 to yield (MA)[$PbBr_3$] (red). C) (MA)[$PbBr_3$] synthesized from Br precursors (blue) and from conversion of (MA)[PbI_3] with Br_2 (red). D) (MA)[$PbCl_3$] synthesized from Cl precursors (blue) and from conversion of (MA)[PbI_3] with sequential Br_2 and Cl_2 (red) and Cl_2 (cyan).

Homogeneous mixed-halide perovskites have intermediate optical and electronic properties that allow for absorbance and emission tuning through synthetic control of the halide composition. Two halide ions that are similar in size allow for uniform perovskite

phases with intermediate halide compositions. For example, Pb-I and Pb-Br form a solid solution (MA)[Pb($I_{1-x}Br_x$)$_3$] and Pb-Br and Pb-Cl form (MA)[Pb($I_{1-x}Cl_x$)$_3$. This allows for facile control over the spectral absorbance for solar-cell absorbers towards optimizing power conversion efficiency in tandem solar cells. Previously, attempts at mixed halide perovskites have used methods where the two halide precursors were deposited simultaneously, creating homogeneous mixtures. Partial conversion of (MA)[PbI_3] using Cl_2 or Br_2 gas allows us to change the halide composition as a function of film depth. This provides a method for forming stratified perovskite film architectures that have not been explored previously. Partial conversion of the (MA)[PbI_3] films can be accomplished by reducing the halogen exposure time. For the Pb-I films that have been partially converted to the Pb-Br perovskite with Br_2, the films show broader PXRD reflections that are intermediate between that of Pb-I and Pb-Br reflections and shallow band absorption. Samples with a greater degree of conversion have diffraction peaks that lie closer to the Pb-Br phase. The peak broadness is likely caused by the solid solution of iodide and bromide causing a gradient bandgap: the composition systematically changes from the iodide-rich phase at the bottom of the film to the bromide-rich phase at the top. In contrast, Pb-I perovskites that were partially converted to the Pb-Cl perovskite with Cl_2 show distinct crystalline phases of pure Pb-I and Pb-Cl perovskites. This indicates that the halides do not mix at intermediate ratios, likely due to the size mismatch between chloride and iodide. Furthermore, two absorption bands are visible in the absorption spectra of these partially converted films. It is likely that greater conversion with either Br_2 or Cl_2 allows for greater penetration of the new halide into the host material.

Progress

We have fabricated 4-terminal hybrid tandem solar cells which comprise of a semi-transparent perovskite solar cell stacked on top of a CIGS or silicon solar cell. The semi-transparent perovskite solar cells have power conversion efficiencies of over 12%. When combined with commercial-grade CIGS solar cells we have achieved power conversion efficiencies of over 18%. This work has enabled the development of the first monolithic silicon-perovskite tandem solar cells that have so far achieved over 13% power conversion efficiency.[41] We have also made substantial advances in understanding degradation pathways in perovskite solar cells due to the presence of electrical bias, light and moisture. Our new 2-dimensional perovskite structures incorporating hydrophobic organic linking groups provide one solution to improving the moisture stability of the perovskite.

We have performed preliminary optical and cost calculations on using perovskite solar cells in hybrid tandems to “upgrade” a conventional silicon solar cell. Monolithically adding a few material layers of the perovskite solar cell on top of a conventional 20% efficient silicon device can increase the device efficiency to over 25% and potentially at an additional cost of only \$10-14/m^2. Assuming that the stability of perovskite solar cells can be improved, perovskite hybrid tandem solar cells have the potential to decrease the cost-per-watt of the current largest market-share solar cells, accelerating the world-wide adoption of solar energy and reducing green-house gases.

Future Plans

The stability of perovskite devices with regards to ion migration in the perovskite poses a significant challenge that may need to be overcome in order to commercialize perovskite hybrid tandem solar cells. We are currently performing electrical measurements on perovskite films to characterize the ionic conductivity of the material and to determine which ions are mobile and the mechanism by which they move. This may help us design suitable barrier layers to prevent electromigration. We are functionalizing the organic groups in these materials to improve their moisture resistance. We are continuing to investigate non-toxic perovskite materials based on germanium as well as bismuth to replace lead. We are also developing deposition methods involving conversion between different perovskite structures and compositions which may result in improved film quality and device performance. These processes also avoid the multi-step conversion process of forming the perovskite and high-temperature vapor annealing steps, which may be less suitable for large scale manufacturing.

Publications and Patents

1. Smith I.C., Hoke E.T., Solis-Ibarra D., McGehee M.D., Karunadasa H.I., A Layered Hybrid Perovskite Solar-Cell Absorber with Enhanced Moisture Stability. Angew. Chemie, 126, 11414–11417, 2014.
2. Unger E.L., Hoke E.T., Bailie C.D., Nguyen W.H., Bowring A.R., Heumuller T., Christoforo M.G., McGehee M.D., Hysteresis and transient behavior in current-voltage measurements of hybrid-perovskite absorber solar cells. Energy Environ. Sci., 7, 3690–3698, 2014.
3. Hoke E.T., Slotcavage D.J., Dohner E.R., Bowring A.R., Karunadasa H.I., McGehee M.D., Reversible photo-induced trap formation in mixed-halide hybrid perovskites for photovoltaics. Chem. Sci., 6, 613–617, 2014.
4. Unger E.L., Bowring A.R., Tassone C.J., Pool V., Gold-Parker A., Cheacharoen R., Stone K.H., Hoke E.T., Toney M.F., McGehee M.D., Chloride in lead-chloride derived organo-metal halides for perovskite-absorber solar cells. Chem. Mater., 26, 7158–7165, 2014.
5. Bailie C.D., Christoforo M.G., Mailoa J.P., Bowring A.R., Unger E.L., Nguyen W.H., Burschka J., Pellet N., Lee J.Z., Grätzel M., et al., Polycrystalline Tandem Photovoltaics Using Perovskites on Top of Silicon and CIGS. Energy Environ. Sci., 8, 956–963, 2015.
6. Solis-Ibarra D., Smith I.C., Karunadasa H.I., Post-synthetic halide conversion and halogen capture in hybrid perovskites. Accepted. Chem. Sci., 2015.

References

1. NREL, Best Research-Cell Efficiencies Chart. http://nrel.gov/ncpv/images/efficiency_chart.jpg, 2015.
2. Jeon N.J., Noh J.H., Kim Y.C., Yang W.S., Ryu S., Seok S. Il, Solvent engineering for high-performance inorganic-organic hybrid perovskite solar cells. Nat. Mater., 13, 897–903, 2014.
3. Jeon N.J., Noh J.H., Yang W.S., Kim Y.C., Ryu S., Seo J., Seok S. Il, Compositional engineering of perovskite materials for high-performance solar cells. Nature, 517, 476–480, 2015.
4. Noh J.H., Im S.H., Heo J.H., Mandal T.N., Seok S. Il, Chemical management for colorful, efficient, and stable inorganic-organic hybrid nanostructured solar cells. Nano Lett., 13, 1764–9, 2013.
5. Smith I.C., Hoke E.T., Solis-Ibarra D., McGehee M.D., Karunadasa H.I., A Layered Hybrid Perovskite Solar-Cell Absorber with Enhanced Moisture Stability. Angew. Chemie, 126, 11414–11417, 2014.
6. Hoke E.T., Slotcavage D.J., Dohner E.R., Bowring A.R., Karunadasa H.I., McGehee M.D., Reversible photo-induced trap formation in mixed-halide hybrid perovskites for photovoltaics. Chem. Sci., 6, 613–617, 2014.

7. Gaynor W., Hofmann S., Christoforo M.G., Sachse C., Mehra S., Salleo A., McGehee M.D., Gather M.C., Lüssem B., Müller-Meskamp L., et al., Color in the corners: ITO-free white OLEDs with angular color stability. Adv. Mater., 25, 4006–13, 2013.
8. Unger E.L., Hoke E.T., Bailie C.D., Nguyen W.H., Bowring A.R., Heumuller T., Christoforo M.G., McGehee M.D., Hysteresis and transient behavior in current-voltage measurements of hybrid-perovskite absorber solar cells. Energy Environ. Sci., 7, 3690–3698, 2014.
9. Ramanathan K., Contreras M.A., Perkins C.L., Asher S., Hasoon F.S., Keane J., Young D., Romero M., Metzger W., Noufi R., et al., Properties of 19.2% efficiency ZnO/CdS/CuInGaSe2 thin-film solar cells. Prog. Photovoltaics Res. Appl., 11, 225–230, 2003.
10. Dualeh A., Moehl T., Tétreault N., Teuscher J., Gao P., Nazeeruddin M.K., Grätzel M., Impedance Spectroscopic Analysis of Lead Iodide Perovskite-Sensitized Solid-State Solar Cells. ACS Nano, 8, 362–373, 2014.
11. Snaith H., Abate A., Ball J., Eperon G.E., Leijtens T., Noel N.K., Stranks S.D., Wang J.T.-W., Wojciechowski K., Zhang W., Anomalous Hysteresis in Perovskite Solar Cells. J. Phys. Chem. Lett., 5, 1511–1515, 2014.
12. Sánchez R.S., Gonzalez-Pedro V., Lee J.-W., Park N.-G., Kang Y.S., Mora-Sero I., Bisquert J., Slow Dynamic Processes in Lead Halide Perovskite Solar Cells. Characteristic Times and Hysteresis. J. Phys. Chem. Lett., doi:10.1021/jz5011187, 2014.
13. Frost J.M., Butler K.T., Walsh A., Molecular ferroelectric contributions to anomalous hysteresis in hybrid perovskite solar cells. APL Mater., 2, 081506, 2014.
14. Mizusaki J., Arai K., Fueki K., Ionic conduction of the perovskite-type halides. Solid State Ionics, 11, 203–211, 1983.
15. Verwey J.F., Time and intensity dependence of the photolysis of lead halides. J. Phys. Chem. Solids, 31, 163–168, 1970.
16. Suarez B., Gonzalez-Pedro V., Ripolles T.S., Sanchez R.S., Otero L., Mora-Sero I., Recombination Study of Combined Halides (Cl, Br, I) Perovskite Solar Cells. J. Phys. Chem. Lett., 5, 1628–1635, 2014.
17. Kulkarni S.A., Baikie T., Boix P.P., Yantara N., Mathews N., Mhaisalkar S., Band-gap tuning of lead halide perovskites using a sequential deposition process. J. Mater. Chem. A, 2, 9221–9225, 2014.
18. Liang P.-W., Liao C.-Y., Chueh C.-C., Zuo F., Williams S.T., Xin X.-K., Lin J., Jen A.K.-Y., Additive Enhanced Crystallization of Solution-Processed Perovskite for Highly Efficient Planar-Heterojunction Solar Cells. Adv. Mater., doi:10.1002/adma.201400231, 2014.
19. Edri E., Kirmayer S., Kulbak M., Hodes G., Cahen D., Chloride Inclusion and Hole Transport Material Doping to Improve Methyl Ammonium Lead Bromide Perovskite-Based High Open-Circuit Voltage Solar Cells. J. Phys. Chem. Lett., 5, 429–433, 2014.
20. Ishii A., Jena A.K., Miyasaka T., Fully crystalline perovskite-perylene hybrid photovoltaic cell capable of 1.2 V output with a minimized voltage lossa). APL Mater., 2, 091102, 2014.
21. Eperon G.E., Stranks S.D., Menelaou C., Johnston M.B., Herz L.M., Snaith H.J., Formamidinium lead trihalide: a broadly tunable perovskite for efficient planar heterojunction solar cells. Energy Environ. Sci., 7, 982, 2014.
22. Sadhanala A., Deschler F., Thomas T.H., Dutton S.E., Goedel K.C., Hanusch F.C., Lai M.L., Steiner U., Bein T., Docampo P., et al., Preparation of Single Phase Films of CH3NH3Pb(I1-xBrx)3 with Sharp Optical Band Edges. J. Phys. Chem. Lett., 5, 2501–2505, 2014.
23. Kuku T., Electrical conductivity of CuSnI3, CuPbI3 and KPbI3. Solid State Ionics, 25, 1–7, 1987.
24. Kuku T., Structure and ionic conductivity of CuCdCl3. Solid State Ionics, 25, 105–108, 1987.
25. Kuku T.., Ionic transport and galvanic cell discharge characteristics of CuPbI3 thin films. Thin Solid Films, 325, 246–250, 1998.
26. Albrecht M.G., Green M., The kinetics of the photolysis of thin films of lead iodide. J. Phys. Chem. Solids, 38, 297–306, 1977.
27. Mitchell J.W., Photographic sensitivity. Reports Prog. Phys., 20, 433–515, 1957.
28. Yin W.-J., Shi T., Yan Y., Unusual defect physics in CH3NH3PbI3 perovskite solar cell absorber. Appl. Phys. Lett., 104, 063903, 2014.
29. Iwanaga M., Azuma J., Shirai M., Tanaka K., Hayashi T., Self-trapped electrons and holes in PbBr2 crystals. Phys. Rev. B, 65, 214306, 2002.

30. Tan Z., Moghaddam R., Lai M., Bright light-emitting diodes based on organometal halide perovskite. Nat. Nanotechnol., doi:10.1038/nnano.2014.149, 2014.
31. Schulz P., Edri E., Kirmayer S., Hodes G., Cahen D., Kahn A., Interface energetics in organo-metal halide perovskite-based photovoltaic cells. Energy Environ. Sci., 7, 1377, 2014.
32. Chen Q., Zhou H., Hong Z., Luo S., Duan H.-S., Wang H.-H., Liu Y., Li G., Yang Y., Planar heterojunction perovskite solar cells via vapor-assisted solution process. J. Am. Chem. Soc., 136, 622–5, 2014.
33. Xing G., Mathews N., Lim S.S., Yantara N., Liu X., Sabba D., Grätzel M., Mhaisalkar S., Sum T.C., Low-temperature solution-processed wavelength-tunable perovskites for lasing. Nat. Mater., 13, 476–80, 2014.
34. Mitzi D.B., Feild C.A., Harrison W.T.A., Guloy A.M., Conducting tin halides with a layered organic-based perovskite structure. Nature, 369, 467–469, 1994.
35. Mitzi D.B., Solution-processed inorganic semiconductors. J. Mater. Chem., 14, 2355, 2004.
36. Shockley W., Quessier H.J., Detailed Balance Limit of Efficiency of P-N Junction Solar Cells. J. Appl. Phys., 32, 510, 1961.
37. Burschka J., Pellet N., Moon S.-J., Humphry-Baker R., Gao P., Nazeeruddin M.K., Grätzel M., Sequential deposition as a route to high-performance perovskite-sensitized solar cells. Nature, 499, 316–9, 2013.
38. Ngo T.T., Chavhan S., Kosta I., Miguel O., Grande H.-J., Tena-Zaera R., Electrodeposition of antimony selenide thin films and application in semiconductor sensitized solar cells. ACS Appl. Mater. Interfaces, 6, 2836–41, 2014.
39. Calixto-Rodriguez M., Garcia H.M., Nair M.T.S., Nair P.K., Antimony Chalcogenide/Lead Selenide Thin Film Solar Cell with 2.5% Conversion Efficiency Prepared by Chemical Deposition. ECS J. Solid State Sci. Technol., 2, Q69–Q73, 2013.
40. Vincent B.R., Robertson K.N., Cameron T.S., Knop O., Alkylammonium lead halides. Part 1. Isolated PbI 6 4− ions in (CH 3 NH 3) 4 PbI 6 •2H 2 O. Can. J. Chem., 65, 1042–1046, 1987.
41. Mailoa J.P., Bailie C.D., Johlin E.C., Hoke E.T., Akey A.J., Nguyen W.H., McGehee M.D., Buonassisi T., A 2-terminal perovskite/silicon multijunction solar cell enabled by a silicon tunnel junction. Appl. Phys. Lett., 106, 121105, 2015.

Contacts

Michael D. McGehee: mmcgehee@stanford.edu
Hemamala Karunadasa: hemamala@stanford.edu
Eric T. Hoke: erichoke@stanford.edu
Colin D. Bailie: cdbailie@stanford.edu
Andrea R. Bowring: bowring@stanford.edu
Rebecca A. Belisle: rbelisle@stanford.edu
Dan Slotcavage: d.slotcavage@stanford.edu
William H. Nguyen: nguyenw@stanford.edu
Ian Smith: ismith9@stanford.edu
Abraham Saldivar: asald@stanford.edu
Adam Slavney: aslavney@stanford.edu
Emma R. Dohner: erdohner@stanford.edu